A Facile Method to Improve the Photocatalytic and Lithium-ion Rechargeable Battery Performance of TiO_2 Nanocrystals

Ting Xia,[1] Wei Zhang,[2] James B. Murowchick,[3] Gao Liu,[2] Xiaobo Chen[1,*]

1. Department of Chemistry, University of Missouri – Kansas City, Kansas City, MO 64110, USA
2. Lawrence Berkeley National Laboratory, Berkeley, CA, 94720, USA.
3. Department of Geosciences, University of Missouri – Kansas City, Kansas City, MO 64110, USA

*Corresponding author:

Xiaobo Chen, phone: 816-235-6420, email: chenxiaobo@umkc.edu

Gao Liu, phone: 510-486-7207, email: GLiu@lbl.gov

KEYWORDS: TiO_2 nanocrystals, photocatalytic properties, lithium-ion rechargeable battery, low-temperature vacuum

ABSTRACT: TiO_2 has been well studied as an ultraviolet (UV) photocatalyst and electrode material for lithium-ion rechargeable batteries, but, with limited optical absorption and lithium-ion storage capacity, respectively. Our recent discovery of hydrogenated black TiO_2 nanocrystals has opened a new avenue towards long-wavelength absorption and has triggered intense research interests for its many applications. However, safety is a concern for the hydrogenation reaction of crystalline TiO_2 under a hydrogen environment at high temperatures. Here we demonstrate that the photocatalytic and the battery performance can be successfully improved with a facile low-temperature vacuum process on the TiO_2 nanocrystals. These TiO_2 nanocrystals extend their optical absorption far into the visible-light region, display nanometer-scale surface atomic rearrangement, possess superoxide ion characteristics at room temperature without light irradiation, show a 4-fold improvement in photocatalytic activity, and 30% better performance in capacity and charge/discharge rates for lithium ion battery. This low-cost, facile method thus could provide an alternative and effective approach in efforts to improve the performance of TiO_2 and other materials towards their practical applications.

1. Introduction

Titanium dioxide (TiO_2) nanomaterials have been widely studied as photocatalysts.[1-6] As TiO_2 only absorbs light in the ultraviolet region, much effort has been devoted in improving the optical and photocatalytic performance of TiO_2, such as by metal or non-metal doping,[7-11] and compositing.[12,13] Our recent discovery of "black" TiO_2 nanoparticles modified by hydrogenation has opened a new avenue towards improvement of long-wavelength optical absorption and high photocatalytic activity,[14] which has triggered great interest.[15-22] Black TiO_2 can be obtained by hydrogenation at elevated temperature from pure white TiO_2 under a high-pressure hydrogen atmosphere.[14] Recent study has shown that hydrogenated TiO_2 performed in an ambient pressure atmosphere consisting of 5 vol% H_2 in Ar displayed better lithium ion battery performance due to the increased electronic conductivity resulted from the increased oxygen vacancy concentration.[20]

Titanium dioxide (TiO_2) has also been studied as an anode material for lithium ion batteries.[23-30] The reaction between lithium and TiO_2 is expressed as:

$$xLi^+ + TiO_2 + xe^- \leftrightarrow Li_xTiO_2$$

where x is the mole fraction of lithium in the titanium dioxide. TiO_2 can offer a capacity up to its theoretical value at 335 $mAhg^{-1}$, or 1.0 Li per TiO_2. For bulk anatase TiO_2, x = 0.5 is usually reported as the maximum.[28,29] High power batteries require fast charge/discharge rates, or fast lithium diffusion rates through the electrode materials. The diffusivity of Li in TiO_2 mostly depends on two major transport processes: the electronic conductivity and the Li^+ diffusivity.[30] However, only a thin

surface layer of the host material is available for Li intercalation at high charging–discharging rates for bulk materials due to the low diffusion coefficient (10^{-11} – 10^{-13} cm^2s^{-1}) and the low electronic conductivity in the solid phase.[26] Conductive secondary phases, such as conductive carbons,[23] carbon nanotubes,[26] graphene,[27] and (with much more improved conductivities) RuO_2,[30] have been used to improve the electronic conduction paths in the host material.

In this study, we demonstrate that the photocatalytic and the battery performance of crystalline TiO_2 nanocrystals can be successfully improved with a facile low-temperature vacuum process. The vacuum-synthesized TiO_2 nanocrystals displayed a four-fold improvement in photocatalytic activity and a 30% improvement in capacity and better rate performance for lithium ion batteries.

2. Results and Discussion

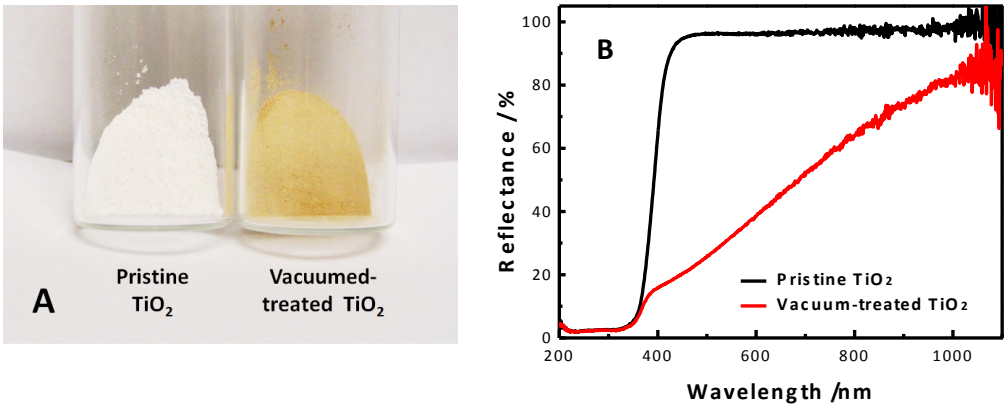

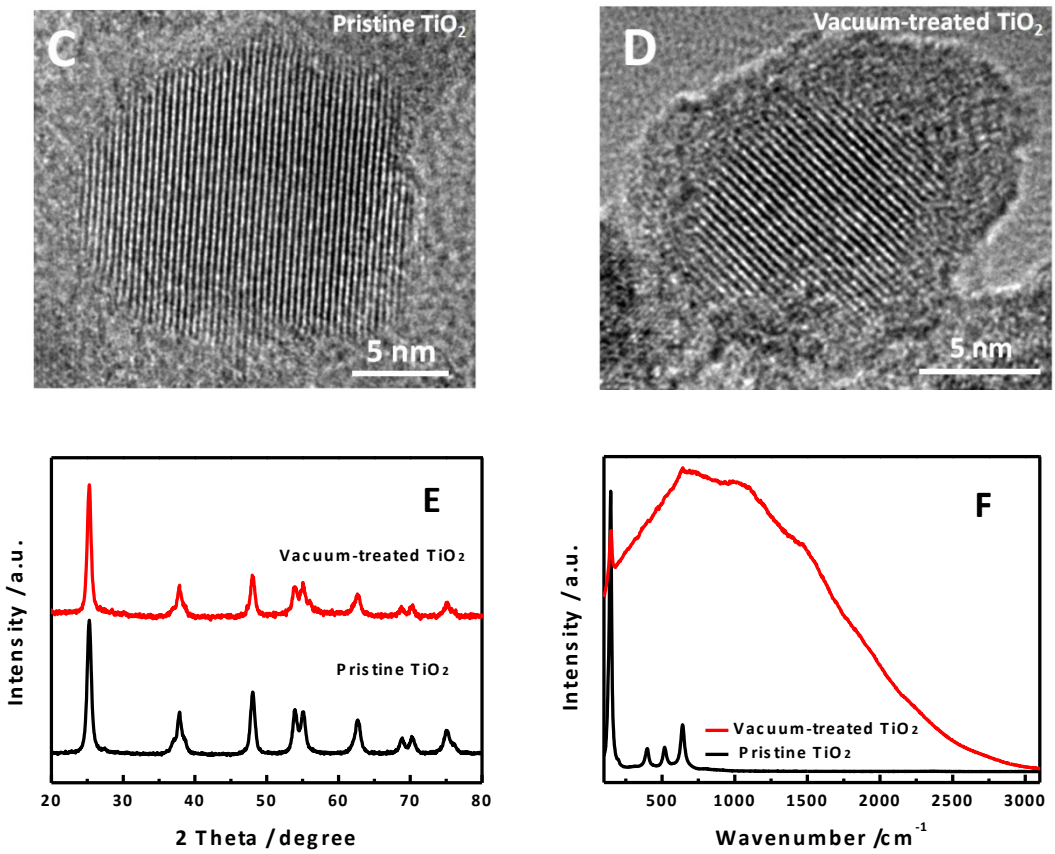

Figure 1. (A) Digital images, (B) UV-vis reflectance spectra, (C) and (D) HRTEM images, (E) XRD results, and (F) Raman spectra of pristine and vacuum-treated TiO_2 nanocrystals.

Vacuum-treated TiO_2 nanocrystals displayed apparent color change to yellow from white pristine TiO_2 nanocrystals (Figure 1A). This suggested that the vacuum-treated TiO_2 nanocrystals had an optical response in the visible light region. Pristine TiO_2 only had absorption in the UV region (< 400 nm), but the vacuum-treated TiO_2 nanocrystals extended their absorption from UV into near infrared (1100 nm) (Figure 1B). Both samples showed particle sizes around 15 nm in diameter as seen from their low-resolution (Supporting information Figure S1) and high-resolution transmission electron microscopy (HRTEM) images (Figures 1C and 1D). Pristine TiO_2 nanocrystals were highly crystalline throughout the whole particle

as indicated by the observed crystalline fringes (Figure 1C), while vacuum-treated TiO_2 nanocrystals displayed a crystalline core with a disordered amorphous shell approximately 2-4 nm thick (Figure 1D). Strong diffraction peaks of both samples suggested that they had highly crystalline anatase phases (Figure 1E). The crystalline domain size was calculated using the Scherrer equation: $\tau = (K\lambda)/(\beta\cos\theta)$, where τ is the mean size of the ordered (crystalline) domains, which may be smaller or equal to the grain size, K is the shape factor with a typical value of 0.9, λ is the X-ray wavelength, β is the line broadening full width at half maximum (FWHM) peak height in radians, and θ is the Bragg angle.[6,22,31] The sizes of both TiO_2 nanocrystals were similar, around 12.0 nm. As Raman spectroscopy is more sensitive to the disordered surface phase, we used it to study both samples. Pristine TiO_2 nanocrystals displayed typical strong and sharp anatase Raman vibrational modes at around 146 cm^{-1} (E_g), 199 cm^{-1} (E_g), 398 cm^{-1} (B_{1g}), 519 cm^{-1} (A_{1g} + B_{1g}), and 642 cm^{-1} (E_g),[14,32-37] but vacuum-treated TiO_2 nanocrystals displayed only a very weak peak around 148 cm^{-1} (E_g) and displayed a large luminescence background (Figure 1E), which are the typical characteristics of an amorphous phase.[33] This verified the existence of the amorphous phase in vacuum-treated TiO_2 nanocrystals observed in the HRTEM images.

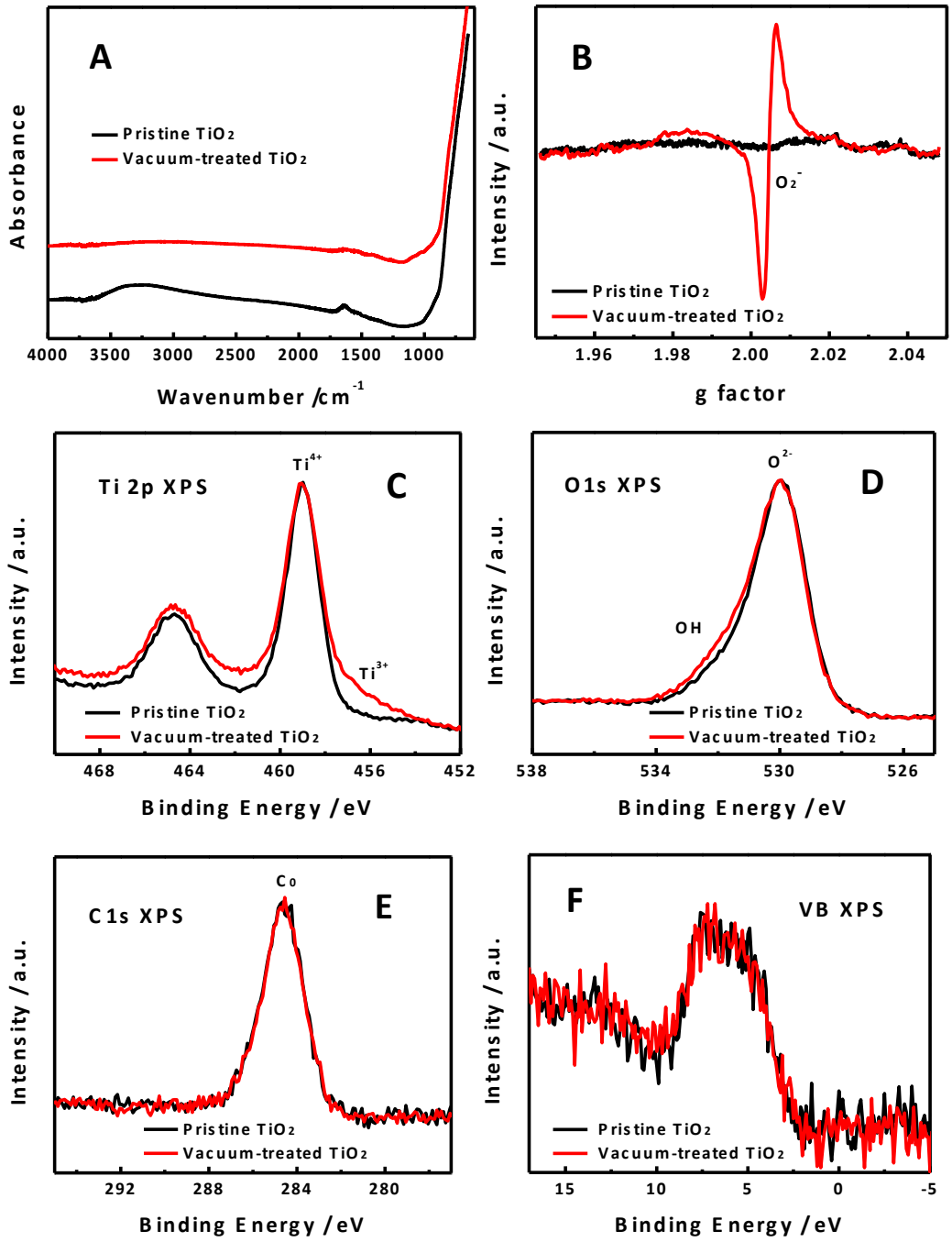

Figure 2. (A) FTIR, (B) ESR, (C)-(F) XPS spectra of pristine and vacuum-treated TiO_2 nanocrystals.

To examine the possible contaminations from any vacuum-oil components, we used Fourier-transformed infrared spectroscopy (FTIR) to see if there were any organic residues from the tubing or sealing material in the oven, although a dry pump was used in the experiments to provide the low-level vacuum of around 1-3 mtorr.

Both TiO_2 nanocrystals displayed similar features: broad-band OH band absorption from 3500 cm^{-1} to 3000 cm^{-1} due to the stretch region of the surface hydroxyl groups and molecularly chemisorbed water,[38-40] band absorption around 1640 cm^{-1} due to the O–H bending of molecularly physisorbed water from the open environment,[38-40] sharp and large O-Ti-O vibrations in the TiO_2 lattice below 1000 cm^{-1} (Figure 2A).[38] No apparent absorption bands were observed for other compounds. This suggests that all the samples are free of possible contaminations.

To examine any creation of free radicals in these nanocrystals, we conducted electron spin resonance (ESR) studies on both samples. The ESR measurements were performed at room temperature and without light irradiation. Pristine TiO_2 nanocrystals did not show any free radical formation characteristics, but vacuum-treated TiO_2 nanocrystals displayed a large response near g factor of 2.004, which was the typical characteristic of superoxide radicals attached to the oxygen vacancy sites in the oxide materials.[41-47] This suggested that oxygen vacancies were generated in the vacuum-treated TiO_2 nanocrystals. It is well known that oxygen vacancies can be created by putting TiO_2 under an ultra-high vacuum environment at high temperatures.[5] The creation of oxygen vacancy in these TiO_2 nanocrystals at low vacuum levels and low temperature could be related to the reduced energies required to remove the oxygen from the lattice due to the nanoscale thermodynamic effect.[48-49] The formation of the oxygen vacancy under the vacuum process can be simply written as using the Kröger-Vink nomenclature:

$2O_O \xrightarrow{vacuum} O_2 + 2V_O^{\cdot\cdot} + 4e^{'}$ where O_O, and $V_O^{\cdot\cdot}$ represent lattice oxygen, and oxygen vacancy, respectively.[50]

To further examine the surface chemical bonding and valence band information, we performed X-ray photoelectron spectroscopy (XPS) measurements on both samples. The positions of the peaks were calibrated to the carbon peak at 284.6 eV. Although both TiO_2 nanocrystals displayed typical Ti 2p core-level XPS spectra with Ti^{4+} characteristics (strong Ti $2p_{3/2}$ peak at binding energy around 459.0 eV and Ti $2p_{1/2}$ near 464.8 eV [9,11,14,17]), vacuum-treated TiO_2 nanocrystals also displayed a shoulder near 457.0 eV, which was characteristic of Ti^{3+}.[9,11] Apparently, Ti^{3+} was also created by the vacuum process in the TiO_2 nanocrystals (Figure 2C). The formation of Ti^{3+} could be associated with the formation of the oxygen vacancy as: $2O_O + Ti_{Ti} \xrightarrow{vacuum} O_2 + 2V_O^{\cdot\cdot} + 3e^{'} + Ti_{Ti}^{'}$ where Ti_{Ti}, and $Ti_{Ti}^{'}$ represent lattice titanium, and Ti^{3+} in the lattice titanium position, respectively.[50] The O 1s core-level XPS spectra of both samples were very similar (Figure 2D): a major peak around 530.0 eV from the O^{2-} ions in the O-Ti-O lattice, and a small shoulder peak around 531.5 eV due to the OH groups on the surface.[11,14,17] Both samples displayed identical C 1s core-level XPS spectra with one peak near 284.6 eV (Figure 2E). The carbon signals were attributed to carbon deposited on the samples from the atmosphere during the XPS measurements. Both samples displayed identical valence band XPS (VBXPS) spectra, and no additional electronic states above pristine TiO_2 nanocrystals were observed for the vacuum-treated TiO_2 nanocrystals (Figure 2F). This is consistent with the conclusion that oxygen vacancy or more likely Ti^{3+} in the

current study caused additional electronic states below the conduction band of pristine TiO_2 crystals, as supported by many previous experimental and theoretical studies.[4,5,17]

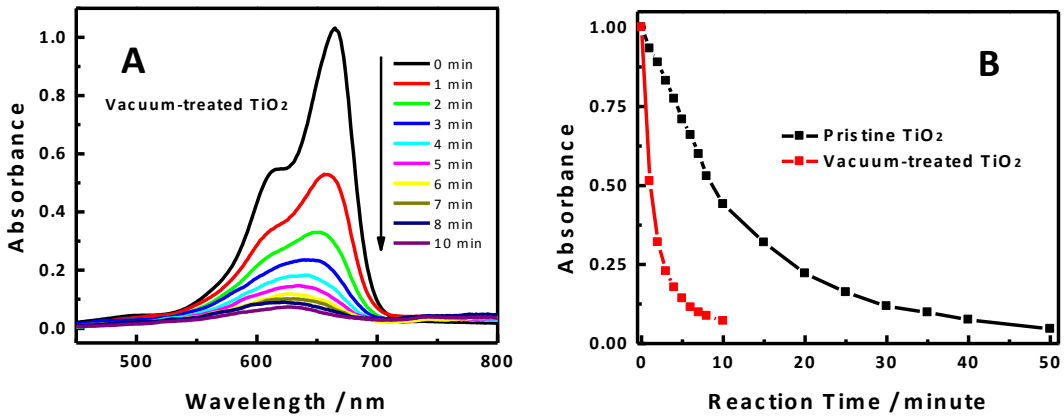

Figure 3. (A) Optical absorbance spectrum change of methylene blue solution under solar irradiation time using vacuum-treated TiO_2 nanocrystals as catalyst. (B) The maximum optical absorbance change of methylene blue solution against solar irradiation time with pristine and vacuum-treated TiO_2 nanocrystals.

To reveal their photocatalytic activity, we conducted photocatalytic decomposition of methylene blue (MB) solution with both samples under simulated solar light irradiation. The methylene blue solution quickly lost its color in the short course of 10 minutes irradiation with the vacuum-treated TiO_2 nanocrystals as catalyst (Figure 3A), indicating most of the methylene blue was decomposed. It took about 40 minutes for the pristine TiO_2 nanocrystals to decompose the same amount of methylene blue molecules under the same condition (Figure 3B). This suggested that vacuum-treated TiO_2 nanocrystals had a four-fold better photocatalytic activity than pristine TiO_2 nanocrystals.

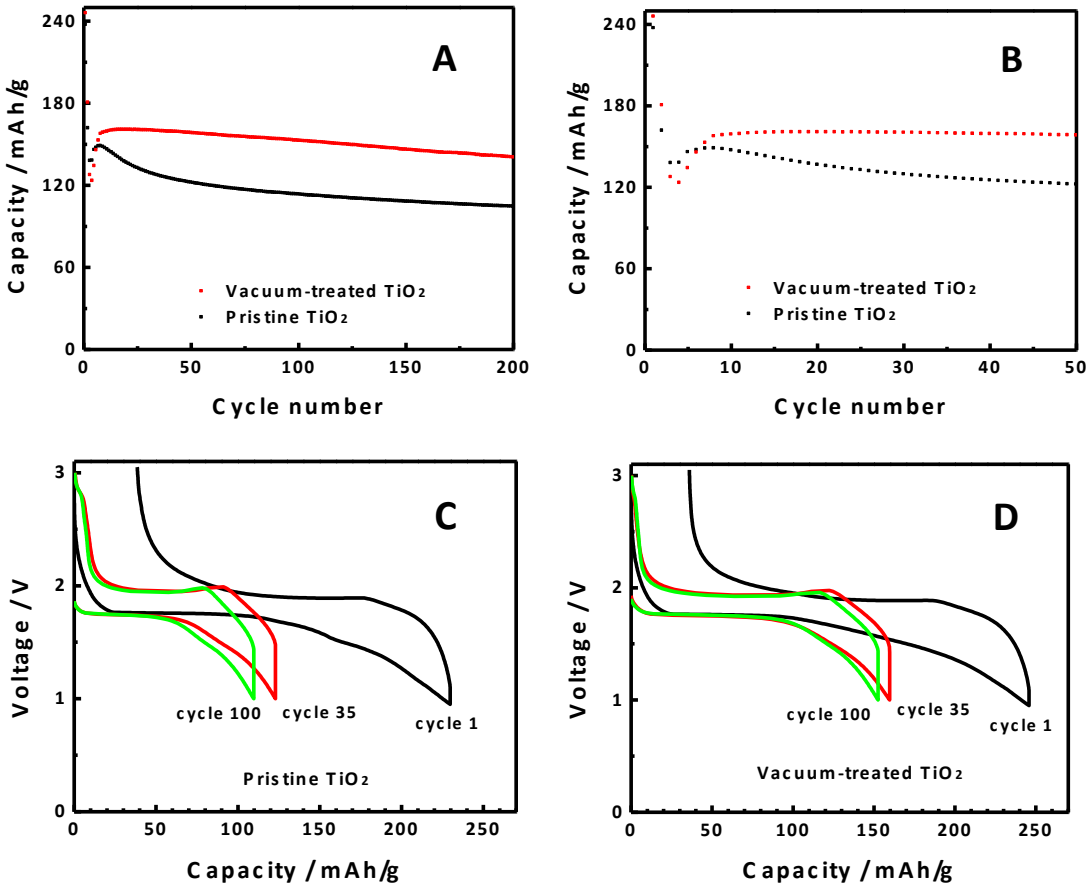

Figure 4. Variation of discharge capacity versus cycle number for pristine and vacuum-treated TiO_2 nanocrystals for the first 200 cycles (A) and the first 50 cycles (B). The first cycle was conducted at C/25 rate, and the second cycle was conducted at C/5 rate, and the remaining cycles were conducted at 1C rate. Galvanostatic charge/discharge profiles for the electrode made of pristine (C) and vacuum-treated (D) TiO_2 nanocrystals at various cycles.

The variation of discharge capacity versus cycle number for the first 200 cycles for pristine and vacuum-treated TiO_2 nanocrystals is shown in Figure 3A. The discharge capacity here corresponds to the Li-insertion process, the discharge of the half-cell, as the TiO_2 was the positive electrode in the half cell. The initial discharge capacity of the vacuum-treated TiO_2 nanocrystals was 246 mAh/g at C/25 rate,

slightly higher than that of the pristine TiO_2 nanocrystals (237 mAh/g). The vacuum-treated TiO_2 nanocrystals displayed lower capacity than the pristine TiO_2 nanocrystals (Figure 3B) in the next four cycles, and then outperformed after the fifth cycle. After 200 cycles, the discharge capacity of the vacuum-treated TiO_2 nanocrystals was 140 mAh/g at 1C rate, 34.5% higher than that of the pristine TiO_2 nanocrystals (104 mAh/g). The discharge capacity of the vacuum-treated TiO_2 nanocrystals decreased almost linearly, while the discharge capacity of the crystalline TiO_2 nanocrystals decreased rapidly in the first 50 cycles and then decreased slowly.

The galvanostatic charge/discharge profiles at first cycle at C/25 rate, 35^{th} cycle at 1C rate, and 100^{th} cycle at 1C rate for the electrode made of the pristine and e vacuum-treated TiO_2 nanocrystals are shown in Figure 3C and Figure 3D. Besides the larger charge/discharge capacity at various cycles, the vacuum-treated TiO_2 nanocrystals show larger charge/discharge plateaus and smaller potential difference between the charge and discharge cycle. For example, the potential difference between the first charge and discharge cycle of the vacuum-treated TiO_2 nanocrystals is about 0.11 V, 42.1% smaller than that of the crystalline TiO_2 nanocrystals of about 0.19 V. This smaller potential difference could hint that the decreased transport resistance and weaker chemical bonds between the host matrix and the Li^+ inserted in the disordered layer, or in other words, due to the higher electronic conductivity of the vacuum annealed samples, possibly associated from the formation of oxygen vacancy [20] and Ti^{3+} as seen from the XPS results. The larger charge/discharge plateaus and smaller potential difference of the vacuum-treated TiO_2 nanocrystals suggest that the

charge transfer is easier than in the vacuum treated TiO_2 nanocrystals.[30,51,52] This can be linked to the increase electronic conductivity due to the formation of the oxygen vacancies reported in the study by Shin et al. as the key to the improvement of electrochemical properties.[20]

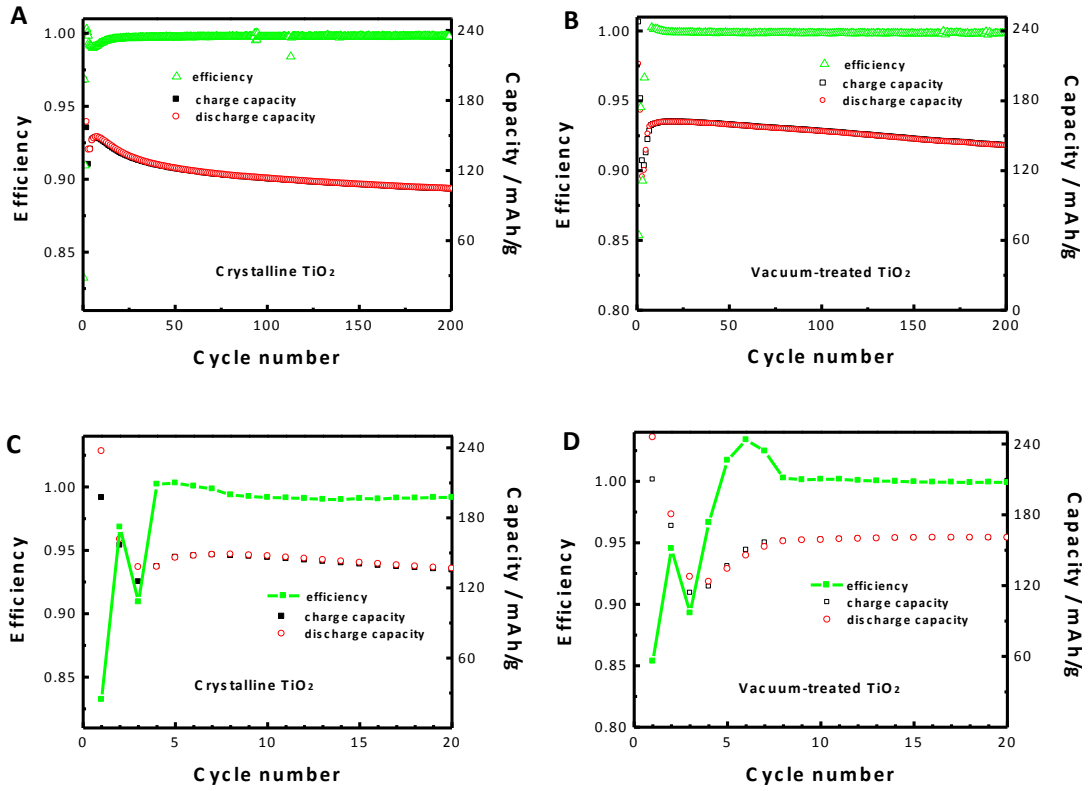

Figure 5. Variation of Coulombic efficiency along with the charge/discharge capacity versus cycle number for the pristine and vacuum-treated TiO_2 nanocrystals for the first 200 cycles (A, B) and 20 cycles (C, D).

Vacuum-treated TiO_2 nanocrystals also displayed higher Coulombic efficiency than the pristine TiO_2 nanocrystals (Figure 5). The first cycle was conducted at C/25 rate, and the second cycle was conducted at C/5 rate, and the remaining cycles were conducted at 1C rate. The pristine crystalline TiO_2 nanocrystals showed a quick drop of the efficiency in the initial stage followed by an increase to around 99.6% after the

first 20 cycles and then remained steady afterward for the remaining 180 cycles (Figure 5A). The efficiency of the vacuum-treated TiO_2 nanocrystals, on the other hand, increased rapidly in the initial few cycles to around 99.9%, and held constant afterward for the remaining 200 cycles (Figure 5B). A closer look at the first 20 cycles revealed that the Coulombic efficiency increased with large fluctuation for the pristine crystalline TiO_2 nanocrystals in the first 4 cycles followed by slight decrease in the next 16 cycles (Figure 5C), while the Coulombic efficiency of the vacuum-treated TiO_2 nanocrystals was slightly lower in the first 4 cycles, then increased rapidly to over unity in cycles 5 to 7, and maintained steadily at the maximum efficiency of 99.9% in the next 16 cycles (Figure 5D). This difference could be due to a larger structural reorganization on the pristine surface for the accommodation of the lithium ions in the formation of the surface electrolyte interface (SEI) layers during the initial cycles of the charge/discharge process. Overall, the vacuum-treated TiO_2 nanocrystals outperformed the pristine crystalline TiO_2 nanocrystals in terms of the Coulombic efficiency in the long run.

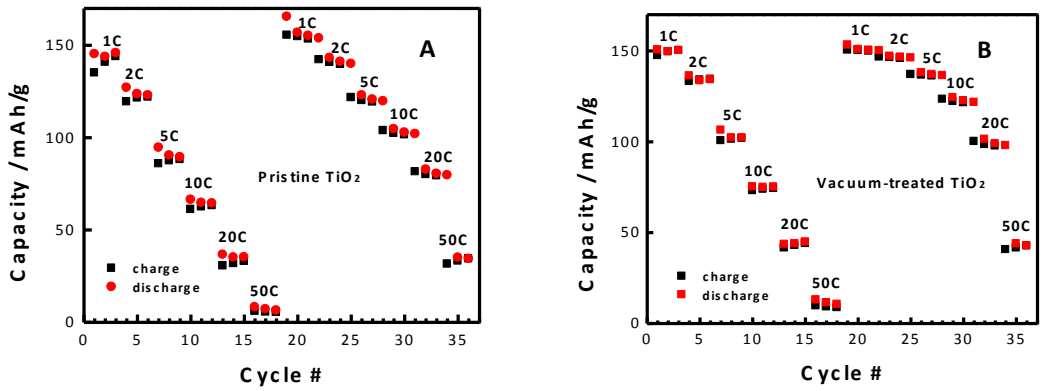

Figure 6. The rate performance of the pristine (A) and vacuum-treated (B) TiO_2 nanocrystals. In the first 18 cycles, the charge and discharge were using the same rate

for each cycle; for the following cycles, the discharge rate was kept at 1C and only the charging rates changed.

Vacuum-treated TiO_2 nanocrystals also showed better rate performance than the pristine TiO_2 nanocrystals (Figure 6). In the first 18 cycles of the testing, the charge and discharge were carried out using the same rates for each cycle; in the following cycles, the discharge rate was kept at 1C and only the charging rate changed. As expected, the mass specific capacity decreases for both samples as the charging/discharging rate increases. For example, the capacity of crystalline TiO_2 decreased from 144 mAh/g (1C) to 65 mAh/g (10C), and 7.1 mAh/g (50C); the capacity of vacuum-treated TiO_2 decreased from 150 mAh/g (1C) to 75 mAh/g (10C) and 12 mAh/g (50C). Apparently, the vacuum-treated TiO_2 nanocrystals show better performance over the crystalline TiO_2 under the same testing condition, i.e. at higher charging/discharging rates. In other words, at the highest charge/discharge rate, 50C, the vacuum-treated TiO_2 displayed 69% capacity increase over crystalline TiO_2. When the discharge rate was kept at 1C and only the charging rate was changed, the discharge capacity of both samples increased, compared to the case where both the charging/discharging rates are the same. Again the discharge capacity of the vacuum-treated TiO_2 is much higher than that of the crystalline TiO_2. For example, at 50C charging rate, the discharge capacity of the vacuum-treated TiO_2 nanocrystal is 44 mAh/g, 26% higher than that of the crystalline TiO_2. The enhancement lithium ion battery performance of the vacuum-treated TiO_2 can be again linked to the fact that

formation of the oxygen vacancies leads to increased electronic conductivity as reported by Shin et al.[20]

3. Conclusions

In summary, we have demonstrated that a vacuum treatment of crystalline TiO_2 nanocrystals at mild temperature and under low-level vacuum can bring about dramatic changes in their structural, optical, electronic and chemical properties. These TiO_2 nanocrystals have displayed much higher photocatalytic activity and improved lithium ion storage performance over the pristine TiO_2 nanocrystals. Thus, this method could provide another way to modify TiO_2 and other oxide nanocrystals in our effort to improve their performance for practical applications.

4. Experimental Section

The pristine TiO_2 nanocrystals were prepared as follows.[14] Briefly, we prepared TiO_2 nanocrystals with a precursor solution consisting of titanium tetraisopropoxide, ethanol, hydrochloric acid, deionized water, and a polymer template, Pluronic F127. The solution was maintained at 40 °C for 24 hours and then dried at 110°C. The dried powders were calcinated in air at 500 °C for 6 hours to obtain pristine TiO_2 nanocrystals. Finally, the pristine TiO_2 nanocrystals were treated under low vacuum of 2-5 mtorr for 4 days at 150 ºC. The vacuum-treated TiO_2 nanocrystals showed yellow color.

The reflectance spectra were collected with an Agilent Cary 60 UV-Vis

spectrometer with an optical reflectance fiber unit. The TEM study was performed on a FEI Tecnai F20 TEM. The electron accelerating voltage was at 200 kV. Small amount of sample was first dispersed in water and then dropped onto TEM grids. The grids were then dried at 60 ºC overnight before TEM examination. The X-ray diffraction (XRD) was performed using a Rigaku Miniflex XRD machine with Cu Kα as the X-ray sources (wavelength = 1.5418 Å) and the 2-theta range was from 15º to 80º with a step width of 0.08 and count time of 3 sec/step. The Raman spectra were collected on an EZRaman-N benchtop Raman spectrometer (Enwave Optronics, Inc.). The Raman spectrometer is equipped with a 300 mW diode laser and the excitation wavelength is 785 nm. The spectrum range was from 100 cm^{-1} to 3100 cm^{-1}. The spectrum collection time was 4 seconds and was averaged over three measurements to improve the signal-to-noise ratio. Fourier-transformed infrared spectroscopy (FTIR) was used to monitor the decomposition process of the sample. The FTIR spectra were collected using a Thermo-Nicolet iS10 FT-IR spectrometer with an attenuated total reflectance (ATR) unit. The electron spin resonance (ESR) spectra were collected on a Benchtop Micro-ESR™ machine. The ESR measurements were done at room temperature without light irradiation. We performed X-ray photoelectron spectroscopy (XPS) measurements on a PHI 5400 XPS system with a conventional (non-monochromatic) Al/Mg Dual-Anode X-ray source. The samples were rolled on graphite conducting tape, and measurements were conducted at $1E^{-9}$ Torr. The positions of the peaks were calibrated to the carbon peak at 284.6 eV.

The photocatalytic activities of the samples were determined by measuring the

photocatalytic decomposition process of methylene blue under simulated solar light irradiation. The solar simulator (81094, Newport) has a 150 watt Xe lamp with an AM 1.5 air mass filter. 1.0 mg of catalyst was added into 3.0 ml methylene blue solution (optical density of 1.0). The UV-vis absorption spectrum of methylene blue was monitored over time after the photocatalytic reaction started. The UV-vis spectrum of methylene blue was measured with an Agilent Cary 60 UV-Vis spectrometer with a spectrum range of from 400 nm to 800 nm.

Half cells were fabricated as follows. The materials used in the fabrication of these half cells included acetylene black (AB), polyvinylidene fluoride (PVDF), N-methylpyrrolidone (NMP) and 1M lithium hexafluorophosphate ($LiPF_6$) in ethylene carbonate (EC): diethyl carbonate (DEC) (1:2 weight ratio). The preparation of the TiO_2 electrodes was conducted in an argon-filled glove box. The electrode mixture (82 wt% TiO_2, 8 wt% AB and 10 wt% PVDF) was steadily dispersed in NMP using a Polytron PT10-35 homogenizer at 2700 rpm for 30 minutes. The slurry was cast on a battery-grade copper sheet using a doctor blade. After being dried overnight, the electrodes were punched to 1/2" diam. discs and dried in *vacuo* at 110°C overnight before being assembled into coin cells. The electrode loading was controlled at around 2.2 mg TiO_2/cm^2.

Coin cell assembly was prepared in standard 2325 hardware under dry argon atmosphere. The separator was from Celgard (product 2400). 1.0 M $LiPF_6$ in 1:2 EC:DEC was used as the electrolyte solution, and lithium as the counter electrode. Cells were discharged to 0.95 V and charged to 3.05 V after 15 min resting for the

first cycle at C/25 (calculated from a specific capacity value of 336 mAh/g) using a Maccor battery cycler at 30°C. For the 2nd cycle, cells were discharged to 1.0 V and charge to 3.0 V at C/5. Then the cells were cycled at 1C from 1.0 V to 3.0 V. One data point was recorded every 10 mV of voltage change. For the first 18 cycles of the rate performance test, the charge and discharge rates were changed simultaneously; and for the following cycles only the charging rates changed while the discharge rate was kept at 1C.

Supporting Information

Supporting Information is available from the Wiley Online Library or from the author.

Acknowledgements

X. C. thanks the support from College of Arts and Sciences, University of Missouri - Kansas City, the University of Missouri Research Board, and the generous gift from Dow Kokam. G. L. thanks the fund by the Assistant Secretary for Energy Efficiency, Office of Vehicle Technologies of the United States Department of Energy under Contract No. DE-AC03-76SF00098.

References

[1] A. Fujishima, K. Honda, *Nature* **1972**, *238*, 37.

[2] A. Fujishima, T. N. Rao, D. A. Tryk, *J. Photochem. Photobiol. C.* **2000**, *1*, 1.

[3] A. L. Linsebigler, G. Lu, J. T. Yates, Jr., *Chem. Rev.* **1995**, *95*, 735.

[4] X. Chen and S. S. Mao, Chem. Rev. **2007**, *107*, 2891.

[5] U. Diebold, *Surf. Sci. Rep.* **2003**, *48*, 53.

[6] T. Xia, J. W. Otto, T. Dutta, J. Murowchick, A. N. Caruso, Z. Peng, X. Chen, *J. Mater. Res.* **2013**, *28*, 326.

[7] W. Choi, A. Termin, M. R. Hoffmann, *J. Phys. Chem.* **1994**, *98*, 13669.

[8] M. Anpo, M. Takeuchi, *J. Catal.* **2003**, *216*, 505.

[9] R. Asahi, T. Morikawa, T. Ohwaki, K. Aoki, Y. Taga, *Science* **2001**, *293*, 269.

[10] S. U. M. Khan, M. Al-Shahry, W. B. Ingler, Jr. *Science* **2002**, *297*, 2243.

[11] X. Chen, C. Burda, *J. Am. Chem. Soc.* **2008**, *130*, 5018.

[12] S. Qian, C. Wang, W. Liu, Y. Zhu, W. Yao, X. Lu, *J. Mater. Chem.* **2011**, *21*, 4945.

[13] D. R. Baker, P. V. Kamat, *Adv. Funct. Mater.* **2009**, *19*, 805.

[14] J. Lu, Y. Dai, H. Jin, B. Huang, *Phys. Chem. Chem. Phys.* **2011**, *13*, 18063.

[15] H. Pan, Y.-W. Zhang, V. B. Shenoy, H. Gao, *J. Phys. Chem. C* **2011**, *115*, 12224.

[16] O. A. Syzgantseva, P. Gonzalez-Navarrete, M. Calatayud, S. Bromley, C. Minot, *J. Phys. Chem. C* **2011**, *115*, 15890.

[17] G. Wang, H. Wang, Y. Ling, Y. Tang, X. Yang, R. C. Fitzmorris, C. Wang, J. Z. Zhang, Y. Li, *Nano Lett.* **2011**, *11*, 3026.

[18] A. Naldoni, M. Allieta, S. Santangelo, M. Marelli, F. Fabbri, S. Cappelli, C. L. Bianchi, R. Psaro, V. D. Santo, *J. Am. Chem. Soc.* **2012**, *134*, 7600.

[19] X. Lu, G. Wang, T. Zhai, M. Yu, J. Gan, Y. Tong, Y. Li, *Nano Lett.* **2012**, *12*, 1690.

[20] J. -Y. Shin, J. H. Joo, D. Samuelis, J. Maier, *Chem. Mater.* **2012**, *24*, 543.

[21] U. Aschauer, A. Selloni, *Phys. Chem. Chem. Phys.* **2012**, *14*, 16595.

[22] T. Xia, X. Chen, *J. Mater. Chem. A*, **2013**, *1*, 2983.

[23] S. Brutti, V. Gentili, H. Menard, B. Scrosati, P. G. Bruce, *Adv. Energy Mater*. **2012**, *2*, 322.

[24] Z. Yang, D. Choi, S. Kerisit, K. M. Rosso, D. Wang, J. Zhang, G. Graff, J. Liu, *J. Power Sources* **2009**, *192*, 588.

[25] M. Wagemaker, A. P. M. Kentgens, F. M. Mulder, *Nature* **2002**, *418*, 397.

[26] I. Moriguchi, R. Hidaka, H. Yamada, T. Kudo, H. Murakami, N. Nakashima, *Adv. Mater.* **2006**, *18*, 69.

[27] N. Li, G. Liu, C. Zhen, F. Li, L. Zhang, H.-M. Cheng, *Adv. Funct. Mater.* **2011**, *21*, 1717.

[28] H. Lindström, S. Södergren, A. Solbrand, H. Rensmo, J. Hjelm, A. Hagfeldt, S.-E. Lindquist, *J. Phys. Chem. B* **1997**, *101*, 7717.

[29] R. van de Krol, A. Goossens, E. A. Meulenkamp, *J. Electrochem. Soc.* **1999**, *146*, 3150.

[30] J. -Y. Shin, D. Samuelis, J. Maier, *Adv. Funct. Mater.* **2011**, *21*, 3464.

[31] *Introduction to X-ray Powder Diffractometry*, ed. R. Jenkins and R. L. Snyder, John Wiley & Sons Inc., New York, 1996.

[32] T. Ohsaka, F. Izumi, Y. Fujiki, *J. Raman Spectr.* **1978**, *7*, 321.

[33] S. Kelly, F. H. Pollak, M. Tomkiewicz, *J. Phys. Chem. B* **1997**, *101*, 2730.

[34] M. Ivanda, S. Musić, M. Gotić, A. Turković, A. M. Tonejc, O. Gamulin, *J. Mol. Struct.* **1999**, *481*, 641.

[35] F. Tian, Y. Zhang, J. Zhang, C. Pan, *J. Phys. Chem. C* **2012**, *116*, 7515.

[36] J. Zhang, M. Li, Z. Feng, J. Chen, C. Li, *J. Phys. Chem. B* **2006**, *110*, 927.

[37] W. Su, J. Zhang, Z. Feng, T. Chen, P. Ying, C. Li *J. Phys. Chem. C* **2008**, *112*, 7710.

[38] J. Zou, J. Gao, F. Xie, *J. Alloys Compd.* **2010**, *497*, 420.

[39] G. Li, L. Li, J. Boerio-Goates, B. F. Woodfield, *J. Am. Chem. Soc.* **2005**, *127*, 8659.

[40] A. T. Kuvarega, R. W. M; Krause, B. B. Mamba, *J. Phys. Chem. C* **2011**, *115*, 22110.

[41] N. Bityurin, A. I. Kuznetsov, A. Kanaev, *Appl. Surf. Sci.* **2005**, *248*, 86.

[42] T. Berger, M. Sterrer, O. Diwald, E. Knözinger, *J. Phys. Chem. B* **2005**, *109*, 6061.

[43] K. Komaguchi, T. Maruoka, H. Nakano, I. Imae, Y. Ooyama, Y. Harima, *J. Phys. Chem. C* **2010**, *114*, 1240.

[44] I. Nakamura, N. Negishi, S. Kutsuna, T. Ihara, S. Sugihara, K. Takeuchi, *J. Molecul. Catal. A* **2000**, *161*, 205.

[45] A. M. Volodin, A. E. Cherkashin, V. S. Zakharenko, *React. Kinet. Catal. Lett.* **1979**, *11*, 103.

[46] J. Ragai, *Nature* **1987**, *325*, 703.

[47] O. I. Micic, Y. Zhang, K. R. Cromack, A. D. Trifunac, M. C. Thurnauer, *J. Phys. Chem.* **1993**, *97*, 72773.

[48] V. Berube, G. Radtke, M. Dresselhaus, G. Chen, *Int. J. Energy Res.* **2007**, *31*, 637.

[49] A. P. Alivisatos, *J. Phys. Chem.* **1996**, *100*, 13226.

[50] *The Defect Chemistry of Metal Oxides*, D. M. Smyth, Oxford University Press, New York, 2000.

[51] H. Morimoto, H. Yamashita, M. Tatsumisago, T. Minami, *J. Am. Ceram. Soc.* **1999**, *82*, 1352.

[52] D. Guan, C. Cai, Y. Wang, *J. Nanosci. Nanotechnol.* **2011**, *11*, 3641.

TOC

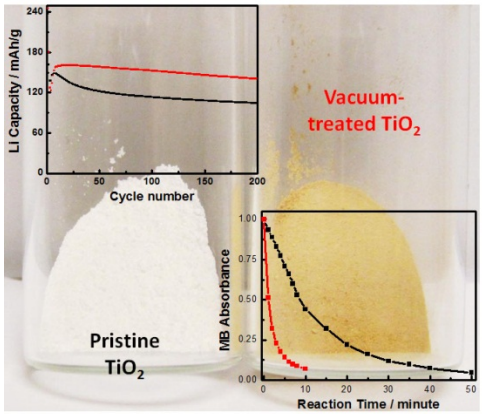

A facile vacuum treatment of TiO_2 nanocrystals largely improved their photocatalytic and lithium-ion battery performances.